IEEE Photonics Journal
An IEEE Photonics Society Publication

Open Access

Coupled Bilayer Photonic Crystal Slab Electro-Optic Spatial Light Modulators

Volume 9, Number 2, April 2017

Yi-Chen Shuai
Deyin Zhao
Yonghao Liu
Corey Stambaugh
John Lawall
Weidong Zhou, *Senior Member, IEEE*

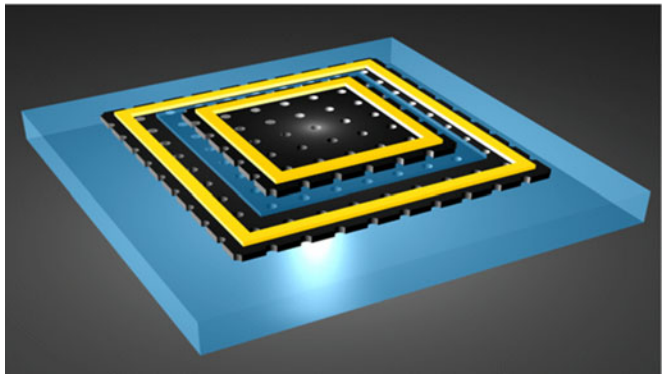

DOI: 10.1109/JPHOT.2017.2675619
1943-0655

IEEE photonics SOCIETY

IEEE

Coupled Bilayer Photonic Crystal Slab Electro-Optic Spatial Light Modulators

Yi-Chen Shuai,[1] Deyin Zhao,[2] Yonghao Liu,[2] Corey Stambaugh,[1] John Lawall,[1] and Weidong Zhou,[2] *Senior Member, IEEE*

[1]National Institute of Standards and Technology, Gaithersburg, MD 20899 USA
[2]Electrical Engineering Department, University of Texas at Arlington, Arlington, TX 76019 USA

DOI:10.1109/JPHOT.2017.2675619

Manuscript received December 15, 2016; revised February 19, 2017; accepted February 23, 2017. Date of publication March 1, 2017; date of current version March 15, 2017. This work was supported by the National Science Foundation through the Physics Frontier Center, Joint Quantum Institute. The work of W. Zhou was supported in part by US ARO (W911NF-15-1-0431, PM: Dr. M. Gerhold), in part by the US AFOSR (FA9550-16-1-0010, PM: Dr. G. Pomrenke), and in part by the NSF (ECCS 1308520).
Corresponding author: W. Zhou (wzhou@uta.edu).

Abstract: We demonstrate here a surface-normal ultracompact Fano resonance electro-optic spatial light modulator employing a stacked photonic crystal membrane capacitor-like structure. Vertically coupled optical resonance near 1.5 μm was observed, and both blue and red spectral shifts were achieved by means of appropriate electrical bias. A 200-MHz modulation bandwidth was obtained on a device with an 80 μm $\times$ 80 μm mesa area, while bandwidths in the gigahertz range are expected by shrinking the mesa lateral size down to 20 μm $\times$ 20 μm. We fabricated 6 $\times$ 6 arrays with different mesa sizes on a silicon-on-insulator platform, illustrating the potential of these devices in vertically integrated photonic technologies and for high-speed spatial light modulations.

Index Terms: Fano resonance, modulators, photonic crystal, free-space optics.

1. Introduction

As one of the most important components in modern communication systems, silicon electro-optical modulators have been realized in a multitude of different configurations [1]. These include widely used Mach-Zehnder interferometer structures [2]–[6], high quality factor (Q) ring resonators [7]–[11], photonic crystal slab (PCS) nanocavities [5], [12], [13], photonic crystal waveguides, and various combinations of these technologies [14]–[16]. In most of the designs studied to date, the light propagates in the plane of the wafer, so as to allow on-chip integration. High speed modulators exceeding 40 GHz have been demonstrated by many groups [3], [17]–[21]. On the other hand, high speed ultra-compact spatial light modulators (SLM), where normal incident light beams are being modulated, are also highly desirable for integrated photonics, including vertically integrated 3-D photonics. They offer opportunities for flexible membrane optoelectronics [22]–[27] which employ 3-D light operation and allow the large-scale integration capability of silicon photonics to serve the 3-D free-space applications [28]. Driven by consumer electronics and the defense industry, SLM technologies are undergoing research and development for modulating the amplitude, phase, or polarization of light waves in space and time. However, these SLMs, which are most often based on liquid crystal (LC) [29]–[31] or micro-electro-mechanical system (MEMS) [32]–[36] technologies,

are relatively slow, with maximum modulation speeds of tens to a few hundreds of kHz for LC [37]–[39] or hundreds of kHz to a few tens of MHz for MEMS [40], [41].

We demonstrate here an ultra-compact electro-optic modulator exploiting a Fano resonance in a coupled bi-layer PCS structure. Our device builds on previous work, in which we demonstrated double-layer Fano resonance high-Q filters with both aligned [42] and displaced [43] PCS lattices. These coupled bi-layer structures are sensitive to small variations in spacing between the two PCS [42], [44], lattice alignment [43], [45] and material refractive index changes on both dielectric layers. This diversity of control mechanisms enables opportunities and applications such as tunable optical high-Q filters, ultra-sensitive molecular and biochemical sensors, optomechanical devices, fast optical switching and electro-optical modulation. Due to its small size and PCS-based vertical structure, this architecture lends itself naturally to an array of modulator pixels. Highly desired for spatial light manipulation, its potential modulation speed can be much faster than LC or MEMS based spatial light modulators.

In this work, we fabricated two kinds of 6 $\times$ 6 membrane device arrays on silicon-on-insulator (SOI) wafer, with square-shaped PCS pattern lateral sizes of 300 μm and 50 μm, respectively. A 200 MHz modulation bandwidth, limited by the parasitic RC time constant, was obtained on individual devices with 50 μm PCS pattern area on the 80 μm mesa. Further shrinking the lateral size of the device will reduce the intrinsic RC time constant to enable gigahertz modulation speeds. While the demonstration presented in this work concerns modulation of the reflection, a straightforward modification of the design would enable it to be used in a transmission mode as well. These coupled bi-layer PCS-based modulators are transferable, stackable, bondable and CMOS compatible. With their small footprint and convenience of 2-D array, they offer a multitude of opportunities for vertical photonic integration and spatial light manipulation.

2. Device Design

The basic idea of the modulator discussed here is illustrated in Fig. 1. Two 230 nm thick silicon photonic crystal slabs, each patterned with an identical square lattice of circular air holes, are separated by a 20 nm layer of SiO_2. The refractive index of silicon is taken to be 3.48 at 1,550 nm spectral band. Notice here both poly-Si and crystalline-Si are used in our experimental demonstrations. The measured index for poly-Si is very similar to the index of crystalline Si. The silicon slabs are P- and N-doped, with the oxide layer providing electrical isolation between them. The lattice period "*a*" is 1 μm and the hole radius "*r*" is 60 nm. These parameters are chosen so as to offer a high quality optical resonance in the 1550 nm wavelength band. The resonance can be excited by surface-normal incident light and the resulting field distribution can be calculated using rigorous coupled-wave analysis. Fig. 1(b) illustrates the electric field distribution of the high-Q resonance, calculated for our parameters using the free software package S4 [46], where periodic boundary condition (PBC) is applied.

Electrical coupling is enabled by the plasma dispersion effect [47]–[49], in which the concentration of the free carriers in silicon changes the real and imaginary parts of the refractive index. This mechanism was studied extensively in silicon [49]. The doping configuration employed in our device is that of a P/Oxide/N structure, comprised of aP-doped (P) bottom layer of crystalline silicon, an electrical isolation layer of thermal SiO_2, and an N-doped (N) top layer of polycrystalline silicon (see Fig. 1(c)). The SiO_2 layer provides electrical isolation between the doped layers, so that the device functions electrically as a parallel-plate capacitor. When a potential difference is imposed between the slabs, the accompanying charge accumulation changes their refractive indices, modifying the optical frequency of the high-Q mode. For a fixed optical frequency, the transmission and reflection are both affected, with slope efficiency proportional to the optical quality factor. We modeled the electrical response of our device in 2-D (*X*-*Y*) using Taurus Medici (Synopsys) [50][1], a semiconductor device simulator. In the simulations, the doping level was taken to 10^{19} cm^{-3} at the

[1]NIST_disclaimer, "Certain commercial equipment, instruments, or materials are identified in this paper in order to specify the experimental procedure adequately. Such identification is not intended to imply recommendation or endorsement by

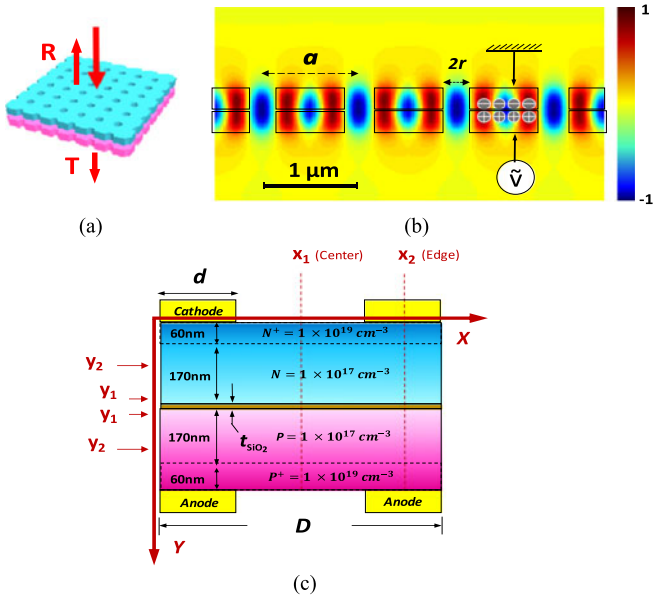

Fig. 1. Three-dimensional sketch of stacked double-layer Photonic Crystal Slabs (PCSs) of 2-D square lattice holes' array was shown in (a). Light incidence from top was reflected or transmitted as the arrows in red. A high resonance mode excited by surface normal incidence was built in the stacked double-layer PCSs. The electrical field intensity was monitored in color as defined from *"-1"* to *"1,"* as shown in (b). In simplified electrical simulation 2-D model (c), electrical bias was applied to the capacitance-like stacked bi-layer PCSs structure for electro-optical modulation. Device lateral size is "*D*" = 20 um, and the electrodes widths are set to be "*d*" = 5 μm. Total thickness of top or bottom Si layer is 60 nm + 170 nm = 230 nm, as shown in (c). The *"t_{SiO2}"* is thickness of SiO_2 between two Si layers. In the X-Y plane, we set a few monitoring positions: " x_1" - center and "x_1" - edge of the device; "y_1"- near Si/SiO_2 interfaces and "y_2"- at middle region of the Si layers.

60 nm outer regions of the silicon slabs and 10^{17} cm^{-3} at the 170 nm inner regions (see Fig. 1(c)). The device width was taken to be $D = 20\,\mu$m limited by the allowed number of grid nodes, and the electrode width to be $d = 5\,\mu$m, as illustrated in Fig. 1(c). The non-uniformity in the electric charge distribution owing to the etched holes was ignored.

2.1 Electrical Simulation

The simulation shows that the free carrier concentrations in Si near the Si/SiO_2 interfaces are strongly modified by electrical carrier injection, defined in Fig. 1(b), resulting in significant local refractive index change as $|\Delta n|$ profiles shown in Fig. 2(a)–(f). Most of the free carrier accumulation occurs near the two interfaces between the conductive Si and the insulating SiO_2 layer; the corresponding perturbation Δn to the refractive index modifies the optical high-Q resonance mode.

The refractive index change ($|\Delta n|$) along Y-axis (depth) corresponding to different SiO_2 layer thicknesses are plotted in Fig. 2(a), under 10 V forward bias with $P = N = 10^{17}$ cm^{-3} doping levels. Larger index change (Δn) can be obtained in thinner oxide case due to carriers concentrating in much smaller volume. Thinner oxide such as 10 nm induces higher absorption, which causes Q factors dropping in optical simulation as shown in Figs. 3(c), (d), and 4(b). Thus an optimized 20 nm SiO_2 thickness was applied for further electrical examination. With the same doping profile (see Fig. 1(b)), Higher (10 V) bias results in higher index change, as shown in Fig. 2(b). Additionally, refractive index changes along *Y*-axis are uniform by comparing index changes at position "x1" (center) and "x2" (edge), as shown in Fig. 2(c). Also the changes in doping concentration (e.g. 10^{17} cm^{-3}

the National Institute of Standards and Technology, nor is it intended to imply that the materials or equipment identified are necessarily the best available for the purpose."

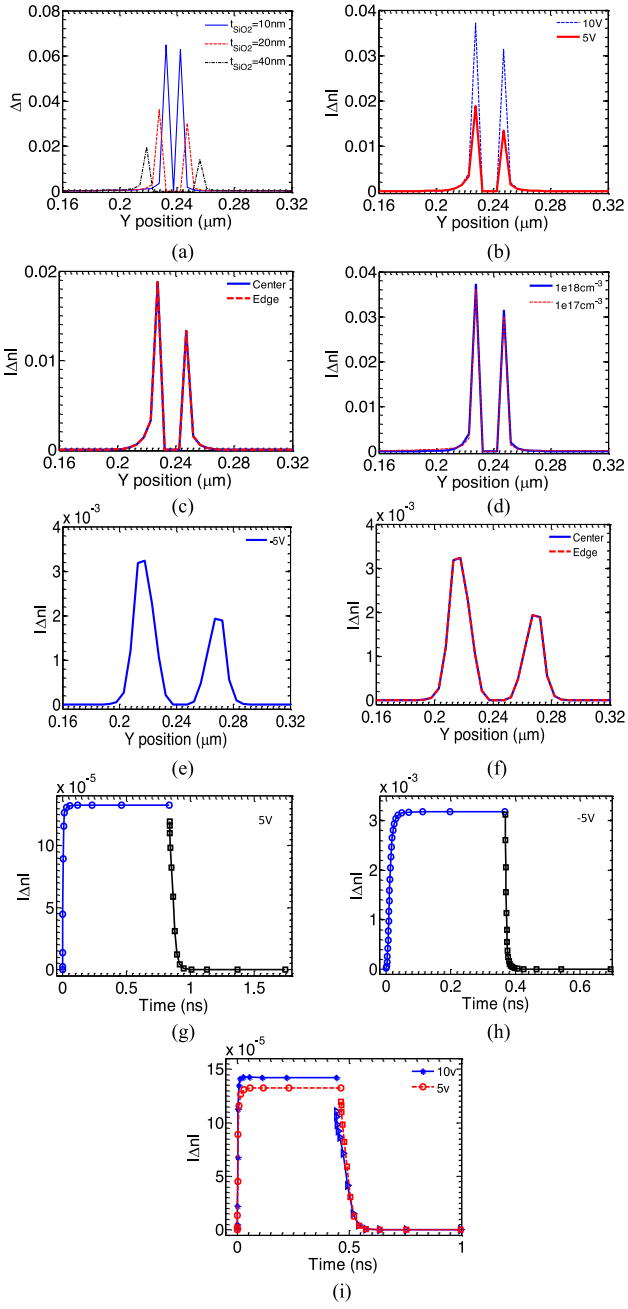

Fig. 2. Simulation results of device electrical performances. Statistic refractive index changes in real part are studied in different cases by comparison, as shown in (a)–(f). Device electrical responses in time domain are also studied, as shown in (g)–(i). These simulation studies are based on the 2-D model shown in Fig. 1(c).

vs $10^{18}\,\mathrm{cm}^{-3}$ as shown in Fig. 2(d)) do not make much difference in refractive index change. Reverse bias cases were also studied with 20 nm sandwiched SiO_2 and $P = N = 10^{17}\,\mathrm{cm}^{-3}$ doping level at the Si inner faces. Under reversed bias of -5 V (Fig. 2(e)), the refractive index change (Δn) is about one order lower than the change under forward bias (see Fig. 2(b)). As expected, $|\Delta n|$ at "x1" (center) and "x2" (edge) are uniform also under reverse bias (see Fig. 2(f)).

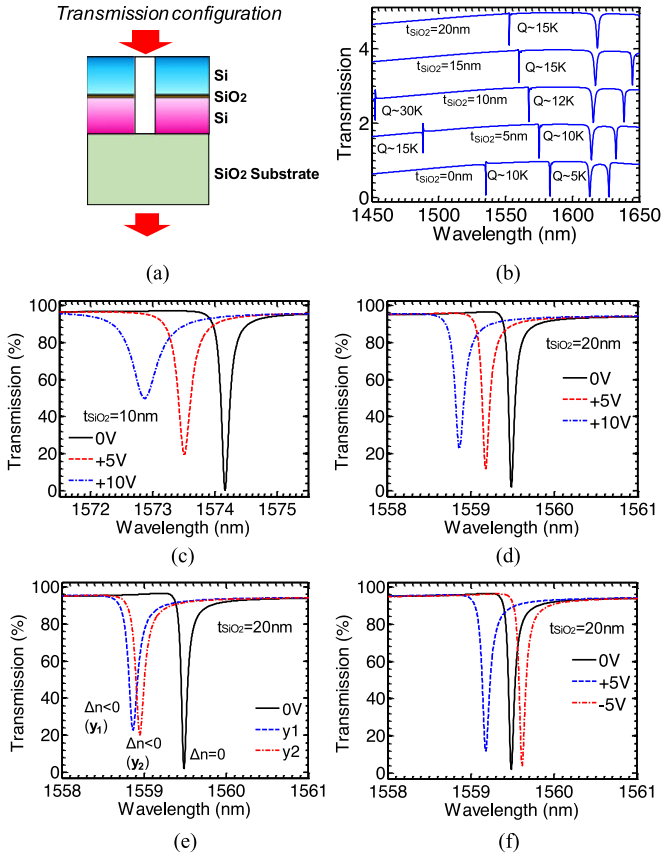

Fig. 3. Device electro-optical (EO) study in transmission configuration: a 2-D sketch of the simulation lattice is shown in (a); for lattice constant "a" $=$ 1 μm and *"r/a"* $=$ 0.08, the transmission spectral centered at 1550 nm is shown in (b) with different sandwiched SiO_2 thicknesses varying from 0 nm to 20 nm. Two different sandwiched SiO_2 thickness, 10 nm in (c) and 20 nm in (d), are also compared for EO spectral shifting. Spectral shifting by free carrier accumulation occurring at either middle or interfaces of Si layers is compared in (e) by 5 V forward bias. Spectral shifting is also compared by 5 V forward/reverse bias, as shown in (f).

In addition to the static study, we calculated the temporal response of the device. As shown in Fig. 2(g)–(i), for an applied forward bias of 5 V, the rise and fall times of $|\Delta n|$ are found to be (30 $\pm$ 5) pico-seconds and (80 $\pm$ 5) pico-seconds, respectively; for reverse bias, the rise and fall times are (30 $\pm$ 5) pico-seconds and (10 $\pm$ 5) pico-seconds. Comparing the forward bias of 5 V to 10 V, the rise and fall times of Δn are similar. These results show the potential of modulation speed measured in GHz for devices with a lateral size of 20 μm.

2.2 Optical Simulation

Optimized device geometry and Si/SiO2/Si layers' thicknesses are determined by systematic investigation and analysis considering many factors in our device model. In the proposed P-type Si/SiO2/N-type Si structure, different sandwiched SiO2 thicknesses and Si doping levels are compared by combination of optical and electrical analysis. Sandwiched SiO_2 thickness of 20 nm was chosen to make a balance between optical and electrical effects. Multiple factors were considered such as: its desired optical Q value, stacked Si/SiO_2/Si layers RC effect, free carrier absorption in Si, effective refractive index changes, sufficient electrical isolation between Si layers, as well as process control preference.

In our optical study, we started from a transmission configuration as in Fig. 3(a). Different SiO_2 thicknesses offer Q-factors varying from 5,000 to 15,000 as shown in Fig. 3(b). Two SiO_2 thickness

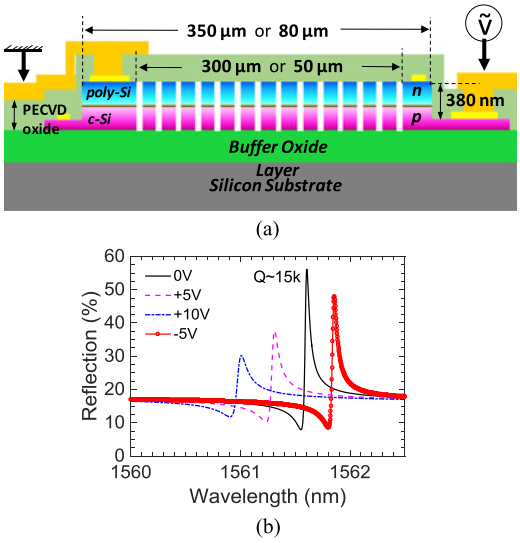

Fig. 4. Device geometry cross-sectional view shows device design with two kinds of lateral dimension (350 μm mesa with 300 μm PC; 80 μm mesa with 50 μm PC) that are investigated in experiments. It has the same sandwiched SiO_2 thickness, *"r"*, *"a"*, Si layer thickness and doping profiles as those applied in transmission configuration (see Fig. 3(d) and (f)). The simulated reflection spectra with different bias are studied in (b) with correspondence to transmission configuration.

cases are compared in Fig. 3(c) and (d) when applying forward bias, the 10 nm oxide case shows larger spectral shifting than 20 nm oxide case, however strong free carrier absorption starts to occur with decreased oxide thickness, resulting in reduced Q factor and extinction ratio. To avoid unintended free carrier absorption and possible thermal effect, 20 nm oxide thickness is determined for later reflection configuration design. It was noticed that, in Fig. 3(e) this interfaces accumulation (as "y_1" positions, in Fig. 1(c)) produces a larger blue shifting on spectra for the resonance mode when comparing to free carrier accumulation appearing in the middle of each Si layer (as "y_2" positions, in Fig. 1(c)). Owing to the semiconductor carrier equilibrium in these two stacked Si PCS, our proposed P/Oxide/N doping structure (see Fig. 1(c)) can be modulated by either forward or reverse bias for blue or red spectral shift respectively, as shown in Fig. 3(f).

A reflection configuration was further investigated by optical simulation. In Fig. 4(a), a 2D sketch shows the device geometry design for two kinds of device sizes. It shows our electrical bias convention. We applied 1 μm buffer oxide layer and 380 nm PECVD oxide for effective reflection spectra as well as for electrical interconnection purposes. Simulation results show a dramatic spectral shifting in Fig. 4(b) when applying electrical bias. It reveals that the free carrier absorption induced extinction ratio and Q-factor decreasing is more critical in reflection configuration.

3. Fabrication and Characterization

We investigated size dependent Q for smaller caviy sizes and we noticed a drop in Q for the cavity size less than 20 μm [51], [52]. For experimental demonstration, we fabricated devices with a somewhat larger lateral size than the simulated one (20 μm lateral size) for better surface-normal light coupling from free space and to facilitate optical alignment during characterization. In practice, we applied two lateral sizes for individual device. Photolithography and reactive ion etching defined a 350 μm $\times$ 350 μm (or 80 μm $\times$ 80 μm) mesa area inside of which e-beam lithography defined a 300 μm $\times$ 300 μm (or 50 μm $\times$ 50 μm) photonic crystal. Fabrication started with a SOI wafer with a 260 nm silicon device layer thickness. A thermal oxide layer was grown on top of the Si. The growth process consumed a 30 nm layer of silicon from the surface, leaving 230 nm. The thermal grown SiO_2 layer was subsequently thinned down to 20 nm by means of a HF wet etching. A polycrystalline silicon layer of 230 nm thickness was deposited atop the thermal oxide layer by means of low-

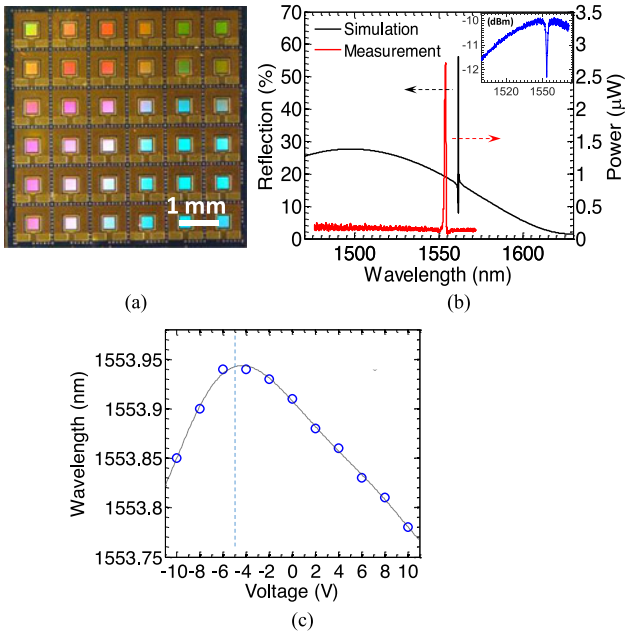

Fig. 5. (a) Microscope top-view image of a 6 × 6 array of 350 μm × 350 μm mesa area devices. (b) Simulated and measured optical resonance mode reflection spectral. Note cross-polarization method is use here for the measured reflection spectrum. Also shown in the inset is the measured reflection spectrum without the using of cross-polarization method. (c) Resonance mode spectral peak shift under electrical bias from −10 V to +10 V.

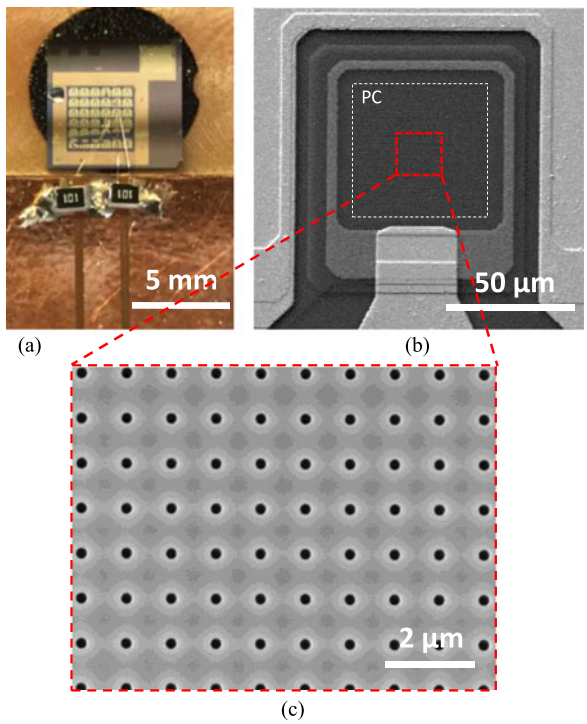

Fig. 6. Die of 6 × 6 array of 80 μm × 80 μm mesa devices is shown in (a); one selected device was wire-bonded to CPW line. In (b), a SEM top-view image for a single modulator device with 80 μm × 80 μm mesa area shows the details of interconnection and electrodes, with a 50 μm × 50 μm PCS area that is defined by the white square dash line. A zoomed-in SEM top-view of its PCS center region is shown on right side in (c).

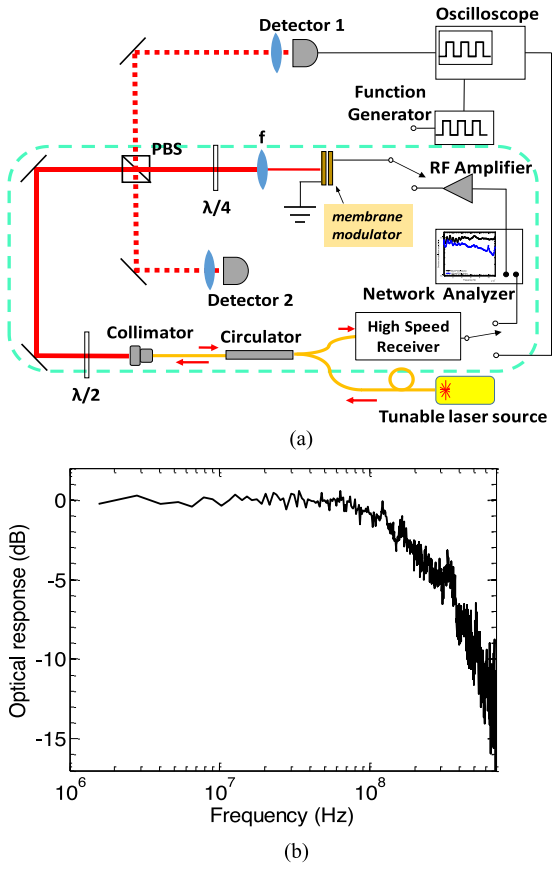

Fig. 7. Characterization setup shown in (a) was used for device optical reflection spectral collection and Electro-Optical (EO) modulation characterization. A network analyzer, RF amplifier, and a high-speed receiver were used for device EO modulation frequency domain characterization. As shown in (b), a 200 MHz 3dB cut-off frequency, which is about 100 times of a 350 μm $\times$ 350 μm mesa area device's performance, was found for the device with 80 μm $\times$ 80 μm mesa area.

pressure chemical vapor deposition. The stacked bi-layers were subsequently boron/phosphorous (P/N) doped by ion implantation into different depths, followed by rapid thermal activation. The array of holes for the photonic crystals was then patterned by electron-beam lithography on a 60 nm Cr layer that is used as a hard mask. The stacked poly-Si/SiO_2/Si layers were etched through to the bottom buffer oxide layer by reactive ion etching, after which the Cr mask was chemically removed. Finally, a 380 nm SiO_2 layer was deposited on top by PECVD for interconnection.

Fig. 5(a) shows a microscope image of a 6 $\times$ 6 array of devices fabricated with 350 μm $\times$ 350 μm mesa area. The optical resonance mode reflection measurement for an individual 350 μm $\times$ 350 μm mesa area device shows a good match to the simulation, as shown in Fig. 5(b).The measured optical power for each wavelength was collected after passing through two crossed polarizers to improve the extinction ratio [53]. Also shown in the inset of the measured reflection spectrum without the using of cross polarizers. Shown in Fig. 5(c) are the measured reflection resonance peak wavelengths for applied electrical biases varying from -10 V to $+10$ V. Notice both spectral blue-shift and red-shift were found when applying forward and reverse bias, respectively. Ideally such shift should be centered at zero bias condition. However, we observed an abnormal blue-shift under large reverse condition (-5 V to -10 V). This could be related to non-uniform carrier concentration change variations in both P and N layers, as well as the non-vertical etched air hole side walls in P and N layers.

A 6 $\times$ 6 array of 80 μm $\times$ 80 μm mesa devices was also fabricated for high frequency EO modulation. It was attached to a dielectric substrate with a coplanar waveguide (CPW) line that was

designed for 10 GHz operation. A single 80 μm $\times$ 80 μm mesa area device was then wire-bonded. The top and bottom electrodes were connected to 150 μm ground/signal pads for wire-bonding. A scanning electron microscope (SEM) top view of a device region with 80 μm $\times$ 80 μm mesa area and a zoomed-in SEM image of the 50 μm $\times$ 50 μm e-beam patterned array of holes, are shown in Fig. 6(b) and (c).

While a modulator such as the one described here can in principle function in either transmission or reflection, we focus on the reflection mode of operation in this work. A schematic diagram of the setup used for tests is shown in Fig. 7(a). Light from a narrow-linewidth tunable laser is sent through a circulator, collimated, and passed through a polarizing beam splitter (PBS) to provide a well-defined linear polarization. The light is focused and directed at the Si-NM device such that the waist of the incident beam falls on the device at normal incidence. A quarter-wave plate can be set with its fast axis parallel to the polarization of the incident light, so that light reflected from the device retraces itself through the collimator and is diverted by the circulator for detection, or with its fast axis at 45 degrees to the incident polarization so that light falling on the device is circularly polarized and the reflected light is deflected by the PBS and subsequently detected.

We supplemented the spectral shifting measurements with frequency-domain EO modulation measurements using a network analyzer. RF amplifier and a high-speed receiver were also used for device EO modulation frequency domain characterization. The predicted optical resonance was found near 1497.5 nm for an 80 μm $\times$ 80 μm mesa area device. For subsequent frequency domain EO modulation tests, the laser wavelength was fixed at 1499 nm where the slope of the reflection spectrum takes its highest value. Fig. 7(b) shows the measured frequency response of the particular 80 μm $\times$ 80 μm mesa device, where 0 dB corresponds to the static (low-frequency) response. As shown in the figure, the response falls off by 3 dB at a frequency of (200 $\pm$ 20) MHz.

4. Conclusion

We have experimentally demonstrated a novel electro-optic intensity modulator exploiting a Fano resonance in a bi-layer photonic crystal architecture. Both blue and red spectral shifts in the resonance were observed, by applying opposite electrical biases. The 3 dB bandwidth of one of our devices, with a lateral size of 80 μm $\times$ 80 μm, was measured to be (200 $\pm$ 20) MHz. These spatial light modulators are polarization independent owing to highly symmetric 2D square lattice photonic crystal structure. Calculations suggest that bandwidths in the GHz range can be achievable if the device size is reduced. High modulation depth should be possible as well, by using a higher optical Q factor PCS stacking structure [42], [43] with process-controlled PCS hole size. These bi-layer coupled PCS-based modulators offer novel opportunities in vertical photonic integration, including free-space communications, 3D optical interconnect, and spatial control of light via extended horizontal arrays.

Acknowledgment

This work was performed in part at the NIST Center for Nanoscale Science and Technology at Gaithersburg. The authors thank Prof. J. Lu at Hunan University in China for sharing his knowledge on device RF packaging, Dr. N. Zimmerman at NIST for useful discussions, and N. Lingaraju for his help with Labview.

References

[1] G. T. Reed, G. Mashanovich, F. Gardes, and D. Thomson, "Silicon optical modulators," *Nature Photon.*, vol. 4, pp. 518–526, 2010.
[2] A. Liu *et al.*, "A high-speed silicon optical modulator based on a metal-oxide-semiconductor capacitor," *Nature*, vol. 427, pp. 615–618, 2004.
[3] A. Liu *et al.*, "High-speed optical modulation based on carrier depletion in a silicon waveguide," *Opt. Exp.*, vol. 15, pp. 660–668, 2007.

[4] M. Y. Liu and S. Y. Chou, "High-modulation-depth and short-cavity-length silicon Fabry–Perot modulator with two grating Bragg reflectors," *Appl. Phys. Lett.*, vol. 68, pp. 170–172, 1996.
[5] B. Schmidt, Q. Xu, J. Shakya, and M. Lipson, "Compact electro-optic modulator on silicon-on-insulator substrates using cavities with ultra-small modal volumes," *Opt. Exp.*, vol. 15, pp. 3140–3148, 2007.
[6] L. Liao *et al.*, "High speed silicon Mach-Zehnder modulator," *Opt. Exp.*, vol. 13, pp. 3129–3135, Apr. 2005.
[7] V. R. Almeida, C. A. Barrios, R. R. Panepucci, and M. Lipson, "All-optical control of light on a silicon chip," *Nature*, vol. 431, pp. 1081–1084, 2004.
[8] Q. Xu, B. Schmidt, S. Pradhan, and M. Lipson, "Micrometre-scale silicon electro-optic modulator," *Nature*, vol. 435, pp. 325–327, 2005.
[9] Q. Xu, B. Schmidt, J. Shakya, and M. Lipson, "Cascaded silicon micro-ring modulators for WDM optical interconnection," *Opt. Exp.*, vol. 14, pp. 9431–9436, 2006.
[10] Y. Vlasov, W. M. Green, and F. Xia, "High-throughput silicon nanophotonic wavelength-insensitive switch for on-chip optical networks," *Nature Photon.*, vol. 2, pp. 242–246, 2008.
[11] P. Dong *et al.*, "Wavelength-tunable silicon microring modulator," *Opt. Exp.*, vol. 18, pp. 10941–10946, 2010.
[12] T. Tanabe, M. Notomi, E. Kuramochi, A. Shinya, and H. Taniyama, "Trapping and delaying photons for one nanosecond in an ultrasmall high-Q photonic-crystal nanocavity," *Nature Photon.*, vol. 1, pp. 49–52, 2007.
[13] A. Majumdar, J. Kim, J. Vuckovic, and F. Wang, "Electrical control of silicon photonic crystal cavity by graphene," *Nano Lett.*, vol. 13, pp. 515–518, 2013.
[14] Y. A. Vlasov, M. O'Boyle, H. F. Hamann, and S. J. McNab, "Active control of slow light on a chip with photonic crystal waveguides," *Nature*, vol. 438, pp. 65–69, 2005.
[15] Y. Jiang, W. Jiang, L. Gu, X. Chen, and R. T. Chen, "80-micron interaction length silicon photonic crystal waveguide modulator," *Appl. Phys. Lett.*, vol. 87, 2005, Art. no. 221105.
[16] T. Baba, "Slow light in photonic crystals," *Nature Photon.*, vol. 2, pp. 465–473, 2008.
[17] X. Xiao *et al.*, "44-Gb/s silicon microring modulators based on zigzag PN junctions," *IEEE Photon. Technol. Lett.*, vol. 24, no. 19, pp. 1712–1714, Oct. 2012.
[18] X. Tu *et al.*, "50-Gb/s silicon optical modulator with traveling-wave electrodes," *Opt. Exp.*, vol. 21, pp. 12776–12782, May 2013.
[19] D. J. Thomson *et al.*, "50-Gb/s silicon optical modulator," *IEEE Photon. Technol. Lett.*, vol. 24, no. 4, pp. 234–236, Feb. 2012.
[20] Y. Tang, J. D. Peters, and J. E. Bowers, "Over 67 GHz bandwidth hybrid silicon electroabsorption modulator with asymmetric segmented electrode for 1.3 μm transmission," *Opt. Exp.*, vol. 20, pp. 11529–11535, May 2012.
[21] P. Dong, C. Xie, L. Chen, L. L. Buhl, and Y.-K. Chen, "112-Gb/s monolithic PDM-QPSK modulator in silicon," *Opt. Exp.*, vol. 20, pp. B624–B629, Dec. 2012.
[22] J. A. Rogers and J.-H. Ahn, *Silicon Nanomembranes: Fundamental Science and Applications*. Hoboken, NJ, USA: Wiley, 2016.
[23] H. Yang *et al.*, "Transfer-printed stacked nanomembrane lasers on silicon," *Nature Photon.*, vol. 6, pp. 615–620, 2012.
[24] W. Zhou *et al.*, "Progress in 2D photonic crystal Fano resonance photonics," *Progress Quantum Electron.*, vol. 38, pp. 1–74, 2014.
[25] J. Yin, X. Cui, X. Wang, P. Sookchoo, M. G. Lagally, and R. Paiella, "Flexible nanomembrane photonic-crystal cavities for tensilely strained-germanium light emission," *Appl. Phys. Lett.*, vol. 108, 2016, Art. no. 241107.
[26] M. Kim, J.-H. Seo, Z. Yu, W. Zhou, and Z. Ma, "Flexible germanium nanomembrane metal-semiconductor-metal photodiodes," *Appl. Phys. Lett.*, vol. 109, 2016, Art. no. 051105.
[27] D. Liu, W. Zhou, and Z. Ma, "Semiconductor nanomembrane-based light-emitting and photodetecting devices," *Photonics*, vol. 3, no. 2, p. 40, 2016.
[28] C. Qiu, J. Chen, Y. Xia, and Q. Xu, "Active dielectric antenna on chip for spatial light modulation," *Sci. Rep.*, vol. 2, p. 855, 2012.
[29] D. Armitage, I. Underwood, and S.-T. Wu, *Introduction to Microdisplays*, vol. 11. Hoboken, NJ, USA: Wiley, 2006.
[30] R. L. Melcher, "LCoS-Microdisplay technology and applications-LCoS is emerging as the most attractive technology choice for a wide variety of portable-and projection-display applications," *Inf. Display*, vol. 16, pp. 20–23, 2000.
[31] G. Lazarev, A. Hermerschmidt, S. Krüger, and S. Osten, *LCOS Spatial Light Modulators: Trends and Applications*. Hoboken, NJ, USA: Wiley-VCH, 2012, pp. 1–30.
[32] M. Doucet, F. Picard, K. K. Niall, and H. Jerominek, "Operation modes for a linear array of optical flexible reflective analog modulators," in *Proc. Defense and Security*, 2005, pp. 219–233.
[33] D. López *et al.*, "Two-dimensional MEMS array for maskless lithography and wavefront modulation," in *Proc. Microtechnologies New Millennium*, 2007, pp. 65890S1–65890S-8.
[34] M. Lapisa, F. Zimmer, F. Niklaus, A. Gehner, and G. Stemme, "CMOS-integrable piston-type micro-mirror array for adaptive optics made of mono-crystalline silicon using 3-D integration," in *Proc. IEEE 22nd Int. Conf. Micro Electro Mech. Syst.*, 2009, pp. 1007–1010.
[35] H. Schenk, A. Wolter, U. Dauderstaedt, A. Gehner, and H. Lakner, "Micro-opto-electro-mechanical systems technology and its impact on photonic applications," *J. Micro/Nanolithography, MEMS, and MOEMS*, vol. 4, 2005, Art. no. 041501.
[36] R. L. Knipe, "Challenges of a digital micromirror device: modeling and design," in *Proc. Lasers, Opt. Vis. Productivity Manufacturing I*, 1996, pp. 135–145.
[37] S. T. Wu and C. S. Wu, "High-speed liquid-crystal modulators using transient nematic effect," *J. Appl. Phys.*, vol. 65, pp. 527–532, 1989.
[38] S. T. Wu, "Nematic liquid crystal modulator with response time less than 100 μs at room temperature," *Appl. Phys. Lett.*, vol. 57, pp. 986–988, 1990.
[39] I. Abdulhalim, G. Moddel, and K. Johnson, "High-speed analog spatial light modulator using a hydrogenated amorphous silicon photosensor and an electroclinic liquid crystal," *Appl. Phys. Lett.*, vol. 55, pp. 1603–1605, 1989.

[40] M. W. Kowarz, J. C. Brazas, and J. G. Phalen, "Conformal grating electromechanical system (GEMS) for high-speed digital light modulation," in *Proc. IEEE 15th Int. Conf. Micro Electro Mech. Syst.*, 2002, pp. 568–573.
[41] J. Suzuki *et al.*, "Micro-mirror On Ribbon-actuator (MOR) for high speed spatial light modulator," in *Proc. IEEE 21st Int. Conf. Micro Electro Mech. Syst.*, 2008, pp. 762–765.
[42] Y. Shuai *et al.*, "Double-layer Fano resonance photonic crystal filters," *Opt. Exp.*, vol. 21, pp. 24582–24589, 2013.
[43] Y. Shuai *et al.*, "Coupled double-layer Fano resonance photonic crystal filters with lattice-displacement," *Appl. Phys. Lett.*, vol. 103, 2013, Art. no. 241106.
[44] V. Liu, M. Povinelli, and S. Fan, "Resonance-enhanced optical forces between coupled photonic crystal slabs," *Opt. Exp.*, vol. 17, pp. 21897–21909, 2009.
[45] W. Suh, O. Solgaard, and S. Fan, "Displacement sensing using evanescent tunneling between guided resonances in photonic crystal slabs," *J. Appl. Phys.*, vol. 98, 2005, Art. no. 033102.
[46] V. Liu and S. Fan, "S 4: A free electromagnetic solver for layered periodic structures," *Comput. Phys. Commun.*, vol. 183, pp. 2233–2244, 2012.
[47] R. S. Jacobsen *et al.*, "Strained silicon as a new electro-optic material," *Nature*, vol. 441, pp. 199–202, 2006.
[48] B. Chmielak *et al.*, "Pockels effect based fully integrated, strained silicon electro-optic modulator," *Opt. Exp.*, vol. 19, pp. 17212–17219, 2011.
[49] R. Soref and B. Bennett, "Electrooptical effects in silicon," *IEEE J. Quantum Electron.*, vol. JQE-23, no. 1, pp. 123–129, Jan. 1987.
[50] Synopsys. (2016). Taurus Medici.
[51] R. R. Boye and R. K. Kostuk, "Investigation of the effect of finite grating size on the performance of guided-mode resonance filters," *Appl. Opt.*, vol. 39, pp. 3649–3653, 2000.
[52] F. Ren, K.-Y. Kim, X. Chong, and A. X. Wang, "Effect of finite metallic grating size on Rayleigh anomaly-surface plasmon polariton resonances," *Opt. Exp.*, vol. 23, pp. 28868–28873, 2015.
[53] Y. Nazirizadeh *et al.*, "Optical characterization of photonic crystal slabs using orthogonally oriented polarization filters," *Opt. Exp.*, vol. 16, pp. 7153–7160, May 2008.